Femtosecond dark-field imaging with an X-ray free electron laser

A.V. Martin,[1,*] N.D. Loh,[2] C.Y. Hampton,[2] R.G. Sierra,[2] F. Wang,[1] A. Aquila,[1,3,4] S. Bajt,[4] M. Barthelmess,[4] C. Bostedt,[2] J.D. Bozek,[2] N. Coppola,[3] S.W. Epp,[5,6] B. Erk,[5,6] H. Fleckenstein,[1] L. Foucar,[5,7] M. Frank,[8] H. Graafsma,[4] L. Gumprecht,[1] A. Hartmann,[9] R. Hartmann,[9] G. Hauser,[10,11] H. Hirsemann,[4] P. Holl,[9] S. Kassemeyer,[7] N. Kimmel,[10,11] M. Liang,[1] L. Lomb,[7] F.R.N.C. Maia,[12] S. Marchesini,[13] K. Nass,[1,14] E. Pedersoli,[15] C. Reich,[9] D. Rolles,[5,7] B. Rudek,[5,6] A. Rudenko,[5,6] J. Schulz,[1,3] R.L. Shoeman,[7] H. Soltau,[9] D. Starodub,[2] J. Steinbrener,[7] F. Stellato,[1] L. Strüder,[10,11] J. Ullrich,[5,6,16] G. Weidenspointner,[10,11] T.A. White,[1] C.B. Wunderer,[4] A. Barty,[1] I. Schlichting,[5,7] M.J. Bogan,[2] and H.N. Chapman[1,14]

[1]*Center for Free-Electron Laser Science, DESY, Notkestrasse 85, 22607 Hamburg, Germany*
[2]*SLAC National Accelerator Laboratory, 2575 Sand Hill Road, Menlo Park, CA 94025, USA*
[3]*European XFEL GmbH, Albert Einstein Ring 19, 22761 Hamburg, Germany*
[4]*Photon Science, DESY, Notkestrasse 85, 22607 Hamburg, Germany*
[5]*Max Planck Advanced Study Group, Center for Free-Electron Laser Science, Notkestrasse 85, 22607 Hamburg, Germany*
[6]*Max-Planck-Institut für Kernphysik, Saupfercheckweg 1, 69117 Heidelberg, Germany*
[7]*Max-Planck-Institut für medizinische Forschung, Jahnstr. 29, 69120 Heidelberg, Germany*
[8]*Lawrence Livermore National Laboratory, 7000 East Avenue, Mail Stop L-211, Livermore, CA 94551, USA*
[9]*PNSensor GmbH, Otto-Hahn-Ring 6, 81739 München, Germany*
[10]*Max-Planck-Institut Halbleiterlabor, Otto-Hahn-Ring 6, 81739 München, Germany*
[11]*Max-Planck-Institut für extraterrestrische Physik, Giessenbachstrasse, 85741 Garching, Germany*
[12]*NERSC, Lawrence Berkeley National Laboratory, Berkeley,California 94720, USA*
[13]*Advanced Light Source, Lawrence Berkeley National Laboratory, Berkeley, California 94720, USA*
[14]*University of Hamburg, Laruper Chausee 149, 22761 Hamburg, Germany*
[15]*Sincrotrone Trieste, Area Science Park, 34149 Trieste, Italy*
[16]*Physikalisch-Technische Bundesanstalt, Bundesallee 100, D-38116 Braunschweig, Germany*
[*]*andrew.martin@desy.de*

#164938 - $15.00 USD Received 23 Mar 2012; revised 21 Apr 2012; accepted 22 Apr 2012; published 31 May 2012

Abstract: The emergence of femtosecond diffractive imaging with X-ray lasers has enabled pioneering structural studies of isolated particles, such as viruses, at nanometer length scales. However, the issue of missing low frequency data significantly limits the potential of X-ray lasers to reveal sub-nanometer details of micrometer-sized samples. We have developed a new technique of dark-field coherent diffractive imaging to simultaneously overcome the missing data issue and enable us to harness the unique contrast mechanisms available in dark-field microscopy. Images of airborne particulate matter (soot) up to two microns in length were obtained using single-shot diffraction patterns obtained at the Linac Coherent Light Source, four times the size of objects previously imaged in similar experiments. This technique opens the door to femtosecond diffractive imaging of a wide range of micrometer-sized materials that exhibit irreproducible complexity down to the nanoscale, including airborne particulate matter, small cells, bacteria and gold-labeled biological samples.

OCIS codes: (110.7440) X-ray imaging; (110.3010) Image reconstruction techniques.

References and links

1. M. M. Seibert, T. Ekeberg, F. R. N. C. Maia, M. Svenda, J. Andreasson, O. Jonsson, D. Odic, B. Iwan, A. Rocker, D. Westphal, M. Hantke, D. P. DePonte, A. Barty, J. Schulz, L. Gumprecht, N. Coppola, A. Aquila, M. Liang, T. A. White, A. Martin, C. Caleman, S. Stern, C. Abergel, V. Seltzer, J.-M. Claverie, C. Bostedt, J. D. Bozek, S. Boutet, A. A. Miahnahri, M. Messerschmidt, J. Krzywinski, G. Williams, K. O. Hodgson, M. J. Bogan, C. Y. Hampton, R. G. Sierra, D. Starodub, I. Andersson, S. Bajt, M. Barthelmess, J. C. H. Spence, P. Fromme, U. Weierstall, R. Kirian, M. Hunter, R. B. Doak, S. Marchesini, S. P. Hau-Riege, M. Frank, R. L. Shoeman, L. Lomb, S. W. Epp, R. Hartmann, D. Rolles, A. Rudenko, C. Schmidt, L. Foucar, N. Kimmel, P. Holl, B. Rudek, B. Erk, A. Homke, C. Reich, D. Pietschner, G. Weidenspointner, L. Struder, G. Hauser, H. Gorke, J. Ullrich, I. Schlichting, S. Herrmann, G. Schaller, F. Schopper, H. Soltau, K.-U. Kuhnel, R. Andritschke, C.-D. Schroter, F. Krasniqi, M. Bott, S. Schorb, D. Rupp, M. Adolph, T. Gorkhover, H. Hirsemann, G. Potdevin, H. Graafsma, B. Nilsson, H. N. Chapman, and J. Hajdu, "Single mimivirus particles intercepted and imaged with an x-ray laser," Nature **470**, 79–81 (2011).
2. A. V. Martin, J. Andreassonn, A. Aquila, S. Bajt, T. R. Barends, M. Barthelmess, A. Barty, W. H. Benner, C. Bostedt, J. D. Bozek, P. Bucksbaum, C. Caleman, N. Coppola, D. P. DePonte, T. Ekeberg, S. W. Epp, B. Erk, G. R. Farquar, H. Fleckenstein, L. Foucar, M. Frank, L. Gumprecht, C. Y. Hampton, M. Hantke, A. Hartmann, E. Hartmann, R. Hartmann, S. P. Hau-Riege, G. Hauser, P. Holl, A. Hoemke, O. Jonssonn, S. Kassemeyer, N. Kimmel, M. Kiskinovak, F. Krasniqi, J. Krzywinski, M. Liang, N.-T. D. Loh, L. Lomb, F. R. N. C. Maia, S. Marchesini, M. Messerschmidt, K. Nass, D. Odic, E. Pedersoli, C. Reich, D. Rolles, B. Rudek, A. Rudenko, C. Schmidt, J. Schulz, M. M. Seibert, R. L. Shoeman, R. G. Sierra, H. Soltau, D. Starodub, J. Steinbrener, F. Stellato, L. Struder, M. Svenda, H. Tobias, J. Ullrich, G. Weidenspointner, D. Westphal, T. A. White, G. Williams, J. Hajdu, I. Schlichting, M. J. Bogan, and H. N. Chapman, "Single particle imaging with soft x-rays at the linac coherent light source," Proc. SPIE **8078**, 807809 (2011).
3. N. D. Loh, C. Y. Hampton, A. V. Martin, D. Starodub, R. G. Sierra, A. Barty, A. Aquila, J. Schulz, L. Lomb, J. Steinbrener, S. Shoeman, R. L. and Kassemeyer, C. Bostedt, J. Bozek, S. W. Epp, B. Erk, R. Hartmann, D. Rolles, A. Rudenko, B. Rudek, L. Foucar, N. Kimmel, G. Weidenspointner, G. Hauser, P. Holl, E. Pedersoli, M. Liang, M. Hunter, L. Gumprecht, N. Coppola, C. Wunderer, H. Graafsma, F. R. N. C. Maia, T. Ekeberg, M. Hantke, H. Fleckenstein, H. Hirsemann, K. Nass, T. A. White, H. J. Tobias, G. R. Farquar, W. H. Benner, S. Hau-Riege, C. Reich, A. Hartmann, H. Soltau, S. Marchesini, S. Bajt, M. Barthelmess, P. Bucksbaum, K. O. Hodgson, L. Strüder, J. Ullrich, M. Frank, I. Schlichting, H. N. Chapman, and M. J. Bogan, "Fractal morphology, imaging and mass spectrometry of single aerosol particles in flight," Nature (2012). (submitted).
4. G. J. Williams, M. A. Pfeifer, I. A. Vartanyants, and I. K. Robinson, "Three-dimensional imaging of microstructure in Au nanocrystals," Phys. Rev. Lett. **90**, 175501 (2003).
5. M. A. Pfeifer, G. J. Williams, I. A. Vartanyants, R. Harder, and I. K. Robinson, "Three-dimensional mapping of a deformation field inside a nanocrystal," Nature **442**, 63–66 (2006).
6. J. Miao, K. O. Hodgson, T. Ishikawa, C. A. Larabell, M. A. LeGros, and Y. Nishino, "Imaging whole Escherichia coli bacteria by using single-particle X-ray diffraction," Proc. Natl. Acad. Sci. USA **100**, 110–112 (2003).

#164938 - $15.00 USD Received 23 Mar 2012; revised 21 Apr 2012; accepted 22 Apr 2012; published 31 May 2012

7. D. Shapiro, P. Thibault, T. Beetz, V. Elser, M. Howells, C. Jacobsen, J. Kirz, E. Lima, H. Miao, A. M. Neiman, and D. Sayre, "Biological imaging by soft X-ray diffraction microscopy," Proc. Natl. Acad. Sci. USA **102**, 15343–15346 (2005).
8. P. Thibault, P. Elser, C. Jacobsen, D. Shapiro, and D. Sayre, "Reconstruction of a yeast cell from x-ray diffraction data," Acta Crystallogr. **A62**, 248–261 (2006).
9. L. Strüder, S. Epp, D. Rolles, R. Hartmann, P. Holl, G. Lutz, H. Soltau, R. Eckart, C. Reich, K. Heinzinger, C. Thamm, A. Rudenko, F. Krasniqi, K.-U. Kühnel, C. Bauer, C.-D. Schröter, R. Moshammer, S. Techert, D. Miessner, M. Porro, O. Hälker, N. Meidinger, N. Kimmel, R. Andritschke, F. Schopper, G. Weidenspointner, A. Ziegler, D. Pietschner, S. Herrmann, U. Pietsch, A. Walenta, W. Leitenberger, C. Bostedt, T. Möller, D. Rupp, M. Adolph, H. Graafsma, H. Hirsemann, K. Gärtner, R. Richter, L. Foucar, R. L. Shoeman, I. Schlichting, and J. Ullrich, "Large-format, high-speed, x-ray pnccds combined with electron and ion imaging spectrometers in a multi purpose chamber for experiments at 4th generation light sources," Nucl. Instrum. Meth. A **614**, 483–496 (2009).
10. XCAM Limited, UK. http://www.xcam.co.uk/documents/XCM_AP_237_1.pdf.
11. H. Philipp, M. Hromalik, M. Tate, L. Koerner, and S. Gruner, "Pixel array detector for x-ray free electron laser experiments." Nucl. Instrum. Meth. A **649**, 67–69 (2011).
12. F. Ottensmeyer, "Macromolecular finestructure by dark field electron microscopy," Biophys. J. **9**, 1144–1149 (1969).
13. F. Ottensmeyer, "Scattered electrons in microscopy and microanalysis," Science **215**, 461–466 (1982).
14. G. Jamjoom, "Dark-field microscopy for detection of malaria in unstained blood films," J. Clin. Microbiol. **17**, 717–721 (1983).
15. A. V. Crewe, J. Wall, and J. Langmore, "Visibility of single atoms," Science **168**, 1338–1340 (1970).
16. J. M. LeBeau, S. D. Findlay, L. J. Allen, and S. Stemmer, "Quantitative atomic resolution scanning transmission electron microscopy," Phys. Rev. Lett. **100**, 206101 (2008).
17. J. Buban, Q. Ramasse, B. Gipson, N. Browning, and H. Strahlberg, "High-resolution low-dose scanning transmission electron microscopy," J. Electron Microsc. **59**, 103–112 (2010).
18. G. R. Morrison and M. T. Browne, "Dark-field imaging with the scanning transmission x-ray microscope," Rev. Sci. Instrum. **63**, 611–614 (1992).
19. H. Chapman, C. Jacobsen, and S. Williams, "A characterisation of dark-field imaging of colloidal gold labels in a scanning transmission x-ray microscope," Ultramicroscopy **62**, 191–213 (1996).
20. J. C. H. Spence, *High-resolution Electron Microscopy* (Oxford University Press, 2003).
21. J. Miao, J. E. Amonette, Y. Nishino, T. Ishikawa, and K. O. Hodgson, "Direct determination of the absolute electron density of nanostructured and disordered materials at sub-10-nm resolution" Phys. Rev. B **68**, 012201 (2003).
22. X. Huang, J. Nelson, J. Steinbrener, J. Kirz, J. Turner, and C. Jacobsen, "Incorrect support and missing center tolerances of phasing algorithms." Opt. Express **18**, 26441–26449 (2010).
23. S. Marchesini, H. He, H. N. Chapman, S. P. Hau-Riege, A. Noy, M. R. Howells, U. Weierstall, and J. C. H. Spence, "X-ray image reconstruction from a diffraction pattern alone," Phys. Rev. B **68**, 140101 (2003).
24. J. R. Fienup, "Phase retrieval algorithms - a comparison," Appl. Opt. **21**, 2758–2769 (1982).
25. C. Jacobsen, J. Kirz, and S. Williams, "Resolution in soft x-ray microscopes." Ultramicroscopy **47**, 55–79 (1992).
26. R. K. Chakrabarty, H. M. Moosmüller, W. P. Arnott, M. A. Garro, and J. Walker, "Structural and fractal properties of particles emitted from spark ignition engines." Environ. Sci. Technol. **40**, 6647–6654 (2006).
27. T. C. Bond and R. W. Bergstrom, "Light absorption by carbonaceous particles: An investigative review," Aerosol Sci. Tech. **40**, 27–67 (2006).
28. M. J. Bogan, D. Starodub, C. Y. Hampton, and R. G. Sierra, "Single-particle coherent diffractive imaging with a soft x-ray free electron laser: towards soot aerosol morphology," J. Phys. B: At. Mol. Opt. Phys. **43**, 194013 (2010).
29. A. V. Martin, F. Wang, N. D. Loh, T. Ekeberg, F. R. N. C. Maia, M. Hantke, G. van der Schot, C. Y. Hampton, R. G. Sierra, A. Aquila, S. Bajt, M. Barthelmess, C. Bostedt, J. D. Bozek, N. Coppola, S. W. Epp, B. Erk, G. R. Farquar, H. Fleckenstein, L. Foucar, M. Frank, L. Gumprecht, A. Hartmann, R. Hartmann, G. Hauser, P. Holl, S. Kassemeyer, N. Kimmel, M. Liang, L. Lomb, S. Marchesini, K. Nass, E. Pedersoli, C. Reich, D. Rolles, B. Rudek, A. Rudenko, J. Schulz, R. L. Shoeman, H. Soltau, D. Starodub, J. Steinbrener, F. Stellato, L. Strüder, J. Ullrich, G. Weidenspointner, T. A. White, C. Wunderer, A. Barty, I. Schlichting, M. J. Bogan, and H. N. Chapman, "Noise-robust coherent diffractive imaging with a single diffraction pattern," Opt. Express (2012). (submitted).

1. Introduction

Coherent diffractive imaging (CDI) at X-ray free-electron lasers (XFELs) is used to image viruses [1, 2] and airborne particulate matter [3] in conditions close to their native state. Viruses can be imaged without staining, freezing or crystallization, and particulate matter can be imaged

#164938 - $15.00 USD Received 23 Mar 2012; revised 21 Apr 2012; accepted 22 Apr 2012; published 31 May 2012

in flight. Additionally, CDI is employed at synchrotrons to image materials science [4, 5] and biological [6, 7] samples as an alternative to full-field and scanning microscopy using X-ray optics. However, CDI techniques developed to date suffer from the ubiquitous issue of missing data [8]. Low spatial frequencies are often not recorded, either because the direct beam is too intense to impact the detector, or because of detector saturation. To reconstruct CDI images with a contrast comparable to a bright-field image the missing data at low frequencies must be recovered through the use of additional constraints or prior knowledge. If there are too many missing speckles, bright-field reconstruction might not be possible.

This issue of missing data is particularly acute for XFEL imaging because the sample is destroyed by a single shot and the dynamic range cannot be extended by repeated measurements of the same sample. The advent of segmented detectors [9–11] for XFEL experiments has further exacerbated the missing data problem. In a recent experiment at the Linac Coherent Light Source (LCLS), the missing data limited reconstructions to particles less than 500 nm in diameter [2]. The size limit arises because the diffraction from larger objects contains variation on finer angular scales than smaller objects. This means the size of the smallest features in a continuous diffraction pattern, commonly known as "speckles", decreases as the object size increases. For a given gap size between detector segments and object-to-detector distance, more information is missing for larger objects making them more difficult to reconstruct. This limit on object size could be increased with a longer object-to-detector distance, but resolution would be sacrificed. Many micrometer-sized samples of high interest, like cells, bacteria and airborne particulate matter (PM), have yet to be imaged with an XFEL at the maximum nano-scale resolution that is potentially achievable. For PM, in particular, the missing data issue restricts the unique opportunities to use XFELs for high spatially and temporally resolved single-particle aerosol dynamics studies of fine particulates, which the EPA designates as particulate matter with an aerodynamic diameter less than 2.5 micron (PM2.5). Our goal is to achieve nanoscale resolution imaging of single particles spanning the entire size range of PM2.5. The upper limit on particle size is currently set by the missing data problem discussed above and the lower limit, about 0.08 micron, is set by scattering cross-section and experimental parameters defining scattered photon detection limits.

Here we show that reconstruction of a dark-field CDI image is a viable route to recovering structural information about the object even when the amount of missing data is severe. Dark-field imaging has been used in electron microscopy to improve the contrast for biological samples without staining [12–14]. Annular dark-field detectors are routinely used in scanning transmission electron microscopy (STEM), where they provide an excellent contrast mechanism for imaging single atoms and atomic columns [15, 16]. Low-dose STEM is being developed for atomic resolution imaging of radiation sensitive samples [17]. Dark-field microscopy has been implemented with X-rays in a scanning transmission X-ray microscope [18] and used for imaging gold-labeled cells [19]. One downside of dark-field imaging is that the image contrast can have a complicated relationship to the object structure and can be difficult to interpret [20].

In a conventional CDI experiment, shown in Fig. 1(a), a far-field diffraction pattern of the sample is collected on the detector, except for a central region where the direct beam is either blocked by a beamstop or passes through a hole. It is commonly assumed that the illumination is fully coherent. Figure 1(a) shows a simulated diffraction pattern for a fractal aggregate, analogous to an airborne soot particle. Using real space constraints like the size and shape of the object (known as a support constraint), the continuous diffraction pattern can be phased to produce an image of soot particle shown in Fig. 1(b) which has an equivalent contrast to a bright-field microscope image. In CDI experiments, a measurement of the direct (unscattered) beam is needed to put the reconstructed transmission of the sample on an absolute scale [21]. Information about the direct beam is usually lost in conventional X-ray CDI experiments be-

#164938 - $15.00 USD Received 23 Mar 2012; revised 21 Apr 2012; accepted 22 Apr 2012; published 31 May 2012

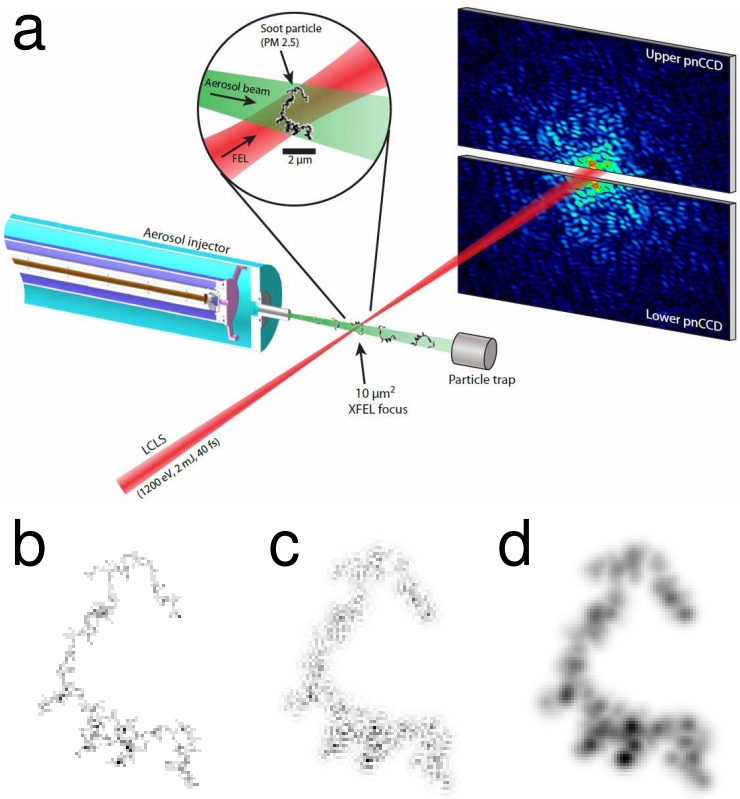

Fig. 1. (a) The CDI experiment at LCLS with a gap between detector halves to prevent the direct beam impinging on the detector. The diffraction pattern is calculated from a simulated soot fractal aggregate. (b) The bright-field image of the soot particle that is formed by conventional CDI. (c) The coherent dark-field image and (d) the incoherent dark-field image.

cause of the beamstop. So conventional CDI reconstructions and bright-field microscopy are not exactly equivalent. However, since the contrast is equivalent we will refer to a CDI reconstruction, where the missing data is recovered, as a bright-field CDI image. Regions of missing data can be uniquely recovered only if there are no unconstrained modes [8]. These modes are functions which are contained within the support and their Fourier transform is contained within the missing data region. They can characterize the structural information that is not constrained by the reconstruction. Until now it was widely believed that it is impossible to reconstruct images from patterns with significant missing central data [22]. Dark field imaging, on the other hand, achieves contrast precisely by omitting low spatial frequency information. The development of dark-field CDI reconstruction methods may therefore enable structural information about the object to be obtained while avoiding the problem of reconstructing the missing data. In principle, the upper limit on the object size that can be imaged would no longer be limited by the missing data region. Dark-field images calculated for coherent (Fig. 1(c)) and incoherent (Fig. 1(d)) illumination of our simulated soot particle suggest that this approach could potentially provide structural information in the CDI experiment.

#164938 - $15.00 USD Received 23 Mar 2012; revised 21 Apr 2012; accepted 22 Apr 2012; published 31 May 2012

2. Theory of dark-field coherent diffractive imaging

To formulate the theory of dark-field CDI reconstruction, we assume that the illumination is fully coherent, so that the scattered wave in the far-field $\psi(\boldsymbol{q})$ can be regarded as a 2D Fourier transform of the scattered wave in the exit surface plane of the object $\psi(\boldsymbol{r})$. The wave recovered by the dark-field reconstruction $\psi_{\text{dark}}(\boldsymbol{r})$ is related to the scattered wave by convolution with a point-spread function $P(\boldsymbol{r})$ as follows

$$\psi_{\text{dark}}(\boldsymbol{r}) = P(\boldsymbol{r}) \otimes \psi(\boldsymbol{r}) \, . \tag{1}$$

The function $P(\boldsymbol{r})$ is determined by the mask $M(\boldsymbol{q})$ that is used multiplicatively to select a subset of the diffraction pattern. The purpose of the mask $M(\boldsymbol{q})$ is not only to specify the location of missing data, but also to ensure that the selected subset of data provides a valid reconstruction problem. It can be easily shown that

$$P(\boldsymbol{r}) = \mathscr{F}\left[\sqrt{M(\boldsymbol{q})}\right] \, , \tag{2}$$

where $\mathscr{F}$ denotes the Fourier transform. The dark-field reconstruction is viable if $\psi_{\text{dark}}(\boldsymbol{r})$ satisfies a support constraint, which depends on the choice of the mask $M(\boldsymbol{q})$. The largest possible choice for $M(\boldsymbol{q})$ is a binary function with a value of one where data is measured and zero where data is missing. However, the sharp edges on such a mask cause $P(\boldsymbol{r})$ to have fringes extending over a wide area, and $\psi_{\text{dark}}(\boldsymbol{r})$ would no longer satisfy a support constraint. A better choice for $M(\boldsymbol{q})$ is a Gaussian mask displaced from the center of the pattern so that it falls to zero in the missing data region. The corresponding $P(\boldsymbol{r})$ is also Gaussian, limiting its spatial extent. The resulting $\psi_{\text{dark}}(\boldsymbol{r})$ is larger than $\psi(\boldsymbol{r})$ but remains of finite size, so a support constraint will be satisfied. For an off-centered mask the associated $P(\boldsymbol{r})$ is complex, so $\psi_{\text{dark}}(\boldsymbol{r})$ cannot be constrained to be real.

By moving the Gaussian mask to different locations, as indicated by the circles in Fig. 2(a), different dark-field images of the soot particle can be reconstructed, as shown in Fig. 2(b)-2(e). Although no data is explicitly removed as "missing data" in this simulation, the choice of mask locations effectively excludes a significant number of central speckles. In this case the reconstruction was performed with shrinkwrap [23] and the hybrid input-output (HIO) method [24]. The contrast of the dark-field image is sensitive to the direction of the displaced Gaussian mask. The square root of the incoherent sum of Fig. 2(b)-2(e) (i.e. the summation of the squares of the amplitude) is shown in Fig. 2(f). The features, although at lower resolution, match those shown in the bright-field reconstruction, Fig. 2(g). Only circular regions from one half of the detector are needed because the diffraction pattern is centrosymmetric.

To ensure the incoherent sum is not biased by the specific directions in which the masks are displaced, the dark-field masks would ideally cover a continuous circle around the center of the pattern (or semi-circle for centrosymmetric patterns). This arrangement has similarities to the annular detectors used in STEM imaging [15]. Practically, there will be limitations on the directions which masks can be displaced given by the geometry of the detector. In this simulation we have avoided horizontally displaced masks to show a similar case to the experimental applications shown Section 3. Aside from avoiding directional bias, the number and placement of masks can be adapted to achieve contrast for the most interesting features of the sample. Since dark-field imaging uses high-frequency information, it is best at displaying fine details of the object structure, such as point-like features and edges.

The contrast of the incoherent sum can be understood from a simple partial coherence model. The off-centered Gaussian mask is written as

$$M(\boldsymbol{q}) = \exp\left[-(\boldsymbol{q}-\boldsymbol{a})^2\sigma^2\right] \, . \tag{3}$$

#164938 - $15.00 USD Received 23 Mar 2012; revised 21 Apr 2012; accepted 22 Apr 2012; published 31 May 2012

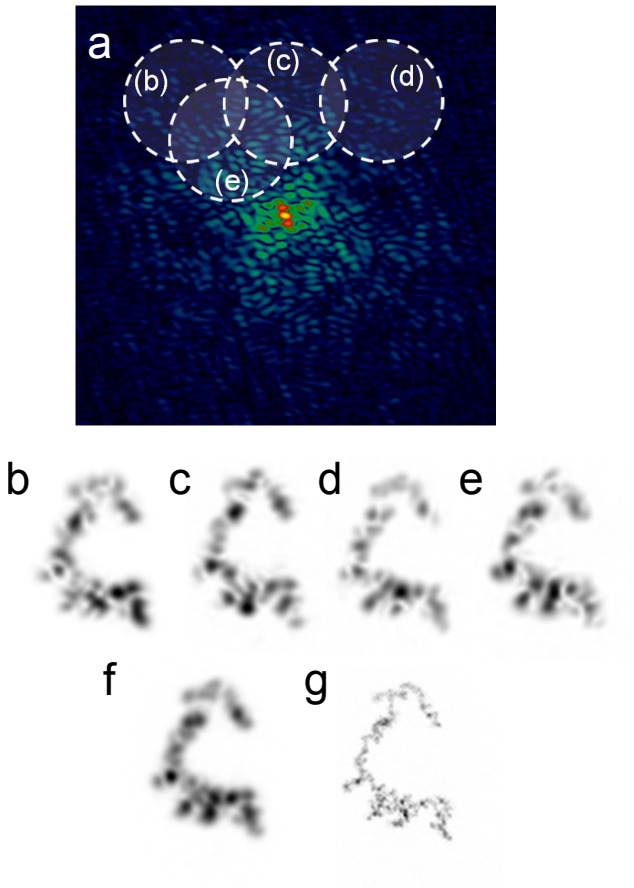

Fig. 2. (a) The simulated diffraction pattern from the model soot fractal aggregate. (b-e) The dark-field reconstructions formed by placing Gaussian masks at the locations indicated by the white circles shown in (a). (f) The incoherent dark-field image formed by adding (b-e) incoherently (the square root is shown so that the contrast is easier to compare). (g) The bright-field reconstruction for comparison.

The corresponding point-spread function is

$$P(\boldsymbol{r}) = \exp\left(-\frac{2\pi^2\boldsymbol{r}^2}{\sigma^2}\right)\exp\left(-2\pi i\boldsymbol{r}\cdot\boldsymbol{a}\right) . \tag{4}$$

By integrating over the displacement vector $\boldsymbol{a}$, the incoherent sum of images can be evaluated

$$\begin{aligned}\int |\psi_{\text{dark}}(\boldsymbol{r})|^2 d\boldsymbol{a} &= \int \left| \int \psi(\boldsymbol{r}') \exp\left[-\frac{2\pi^2(\boldsymbol{r}-\boldsymbol{r}')^2}{\sigma^2}\right] \exp\left[-2\pi i(\boldsymbol{r}-\boldsymbol{r}')\cdot\boldsymbol{a}\right] d\boldsymbol{r}' \right|^2 d\boldsymbol{a} \\ &= \int |\psi(\boldsymbol{r}')|^2 \exp\left[-\frac{4\pi^2(\boldsymbol{r}-\boldsymbol{r}')^2}{\sigma^2}\right] d\boldsymbol{r}' \\ &= |\psi(\boldsymbol{r})|^2 \otimes |P(\boldsymbol{r})|^2 . \end{aligned} \tag{5}$$

Hence, in this model the incoherently-summed dark-field intensity is equivalent to the bright-field intensity convolved with a Gaussian point-spread function. Resolution is lost but contrast

#164938 - $15.00 USD Received 23 Mar 2012; revised 21 Apr 2012; accepted 22 Apr 2012; published 31 May 2012

is preserved. Since the width of $|P(\boldsymbol{r})|^2$ in Eq. (5) is a factor of $\sqrt{2}$ smaller than $|P(\boldsymbol{r})|$, the resolution of the incoherent image is better than that of a coherent image, a principle that is well-known in X-ray microscopy [25]. For dark-field CDI, we only use values of $\boldsymbol{a}$ that avoid the beamstop or detector gaps, so Eq. (5) does not apply exactly. The aim is to add enough dark-field images to approach the contrast of Fig. 1(d), which, as Fig. 2(f) shows, can be achieved with only a few reconstructions.

A notable advantage of this formulation of dark-field CDI is that it requires no modification of the experimental set up and can be applied to existing data that has been regarded up until now as unusable.

3. Experiment

Dark-field CDI was used to study soot particles, which belong to the high-interest PM2.5 category of particular matter. The structure and size of these heterogeneous particles determines their optical and transport properties, which are an important, yet still uncertain, aspect of climate modeling, and also determines their toxicological effects via respiration [26,27]. However, transmission electron microscopy (TEM) and scanning transmission microscopy (STM) have the disadvantages of slow data collection, particle melting, and the need to capture the particle on a substrate [26]. XFELs have the unique opportunity to study large ensembles of this heterogeneous sample by taking individual measurements of each particle while still airborne.

The diffraction data was taken at the Atomic, Molecular and Optics beamline at the LCLS. The sample was a soot particle generated from a Palas GFG1000 spark source generator (Karlsruhe, Germany), which was injected into the FEL beam as an aerosol through a differentially pumped aerodynamic focusing inlet [28]. Individual particles were exposed to vacuum for 1 ms as they traveled at 100-200 m/s to the interaction region. The incident photons had an energy of 1.24 keV (wavelength of 1.0 nm). The diffraction pattern was recorded on a pnCCD detector which was installed in the CFEL ASG Multi-Purpose (CAMP) instrument [9]. The dynamic range of the detector as operated in this experiment was approximately 500 photons and there is a 3 mm radius hole in the center to allow the direct beam to pass. The detector was approximately 724 mm from the interaction region. Further parameters and details of the LCLS experiment are given by Loh et al. [3].

Our aim is to form a dark-field image by taking the incoherent sum of dark-field images associated with Gaussian masks in different locations. Two different methods were implemented to form the incoherent dark-field images from the experimental data. Method A is exactly what was implemented in the simulation already described. It is as follows:

1. Perform a separate reconstruction for each Gaussian mask.
2. Take the incoherent sum of each of these dark-field reconstructions.

Method B involves a single reconstruction from a larger mask:

1. Add the Gaussians to form a single mask.
2. Perform a single reconstruction from data masked with the combined mask.
3. Construct the incoherent dark-field image by post-processing the reconstructed wave. Each Gaussian mask is applied separately to the reconstructed wave to generate a series of dark-field images, which are then summed to form the incoherent dark-field image.

In both Methods A and B, the term “reconstruction” can be any standard CDI reconstruction procedure. The specific details of the procedure that we used is given below, after we discuss the merits of Methods A and B.

#164938 - $15.00 USD Received 23 Mar 2012; revised 21 Apr 2012; accepted 22 Apr 2012; published 31 May 2012

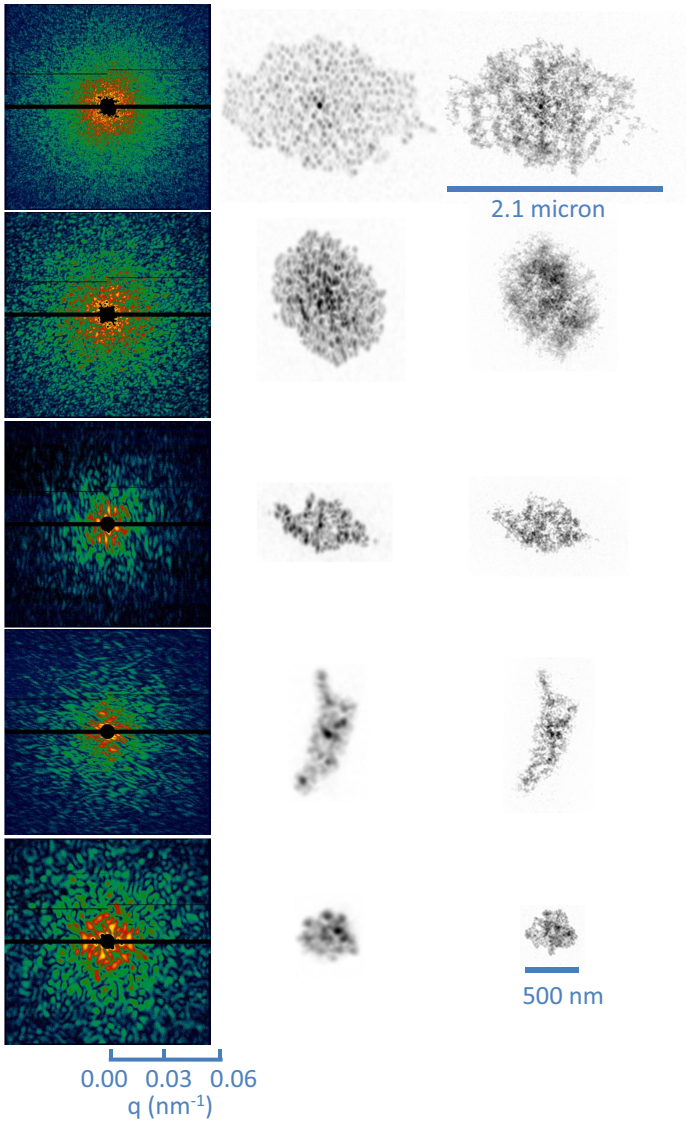

Fig. 3. On the left are the measured diffraction patterns. The black region is where data was not recorded due to the central hole, the gap between the two detector halves or saturation. The dark-field reconstructions are shown in the center. The dark-field reconstruction provided a support and initial starting point which were needed to obtain the bright-field reconstructions shown on the right.

Method A is how we first conceived dark-field imaging and what we initially implemented. It was successful on the diffraction patterns for smaller samples and was used to produce the results for the two bottom particles in Column 2 of Fig. 3. Five Gaussian masks were used similar to those that were successful in simulation. The radius of the Gaussian masks was 60 pixels or 6×10^3 nm^{-1} and the full-period resolution of the dark-field reconstruction using Method A was approximately 170 nm.

For larger particles, Method A was found to be more greatly affected by noise and was not

#164938 - $15.00 USD Received 23 Mar 2012; revised 21 Apr 2012; accepted 22 Apr 2012; published 31 May 2012

reliable. We attribute this to the fact that the oversampling of larger particles is less than for smaller particles, and the effective signal-to-noise ratio per speckle is comparatively greater. To overcome this problem, Method B was developed. By performing a single reconstruction from a larger mask, the effective signal-to-noise level in the object plane is reduced (as each pixel in the estimated image of the object is calculated using more diffraction data). Furthermore, Method B is faster because it requires fewer reconstructions. Method B was successful at reconstructing the top three images shown in Fig 3. More Gaussians can be added in Method B without increasing computational time, and so the number of Gaussians was increased to seven to use more data. For the reconstructions using method B, the radius of the Gaussian masks was also 60 pixels. However, in Method B we also have the flexibility to use Gaussian masks of different widths in steps (1) and (3). Taking advantage of this, the size of the Gaussian mask in step (3) of Method B was increased to 1×10^4 nm^{-1}, so the full-period resolution of the final incoherent image was approximately 100 nm.

The reconstruction step, in Method A or B, can be implemented with any standard CDI reconstruction procedure. We found there were issues with noise sensitivity when using standard methods like HIO with this data. To overcome this issue, standard hybrid input-output method (HIO) was modified to improve noise tolerance. The iterative scheme is as follows:

$$\psi^{(n+1)} = \begin{cases} P_{\text{mod}}\psi^{(n)}, & \in S \\ \psi^{(n)} - \beta P_{\text{mod}}\psi^{(n)}, & \notin S \bigcap |P_{\text{mod}}\psi^{(n)}| > m, \\ 0, & \notin S \bigcap |P_{\text{mod}}\psi^{(n)}| \leq m\,, \end{cases} \tag{6}$$

where S denotes the support, β is a feedback parameter set to 0.9, and P_{mod} is the modulus projection operator given by

$$P_{\text{mod}}\psi = \mathscr{F}^{-1}\left\{\sqrt{I}\exp\left[i\arg(\mathscr{F}[\psi])\right]\right\}\,, \tag{7}$$

where I is the measured diffraction pattern. The threshold m was set according to the noise level in the autocorrelation function. A detailed description of the formulation and properties of this method are to be published in a separate manuscript [29]. Shrinkwrap [23] was used to dynamically calculate the support using a threshold every 50 iterations. The threshold is applied after smoothing the current iterate with a Gaussian kernal whose width is gradually reduced during reconstruction. The initial width of the kernal was chosen in the range of 2.0–5.0 pixels full-width-half-maximum and the final width was 1.0 pixel full-width-half-maximum. For reconstructions in Method A the diffraction data was noise filtered after applying the dark-field mask. Noise filtering involved the application of a support to the autocorrelation function, calculated by the same method as in Shrinkwrap. For the reconstructions in Method B, this additional noise filtering was not required as the the use of a larger mask improved the robustness to noise.

To ensure reliability of a CDI reconstruction, it is common procedure to take the average of separate trials made from different random starting points. Each dark-field reconstruction shown here is an average of ten trials and each trial was set to run for a fixed number of iterations. For these small objects which had the largest speckles, each trial for reconstructions in Method A converged in a few hundred iterations (300–500). Reconstructions of the larger particles with the larger mask from Method B were slower and the number of iterations needed for convergence was within the range 5000–25000 iterations. After a successful reconstruction was achieved in each case, finding the minimum number of iterations required was not considered a priority, and so these numbers only represent a rough estimate of what is minimally required.

The reconstructed dark-field images in the central column of Fig. 3 show the shape and size of the soot particles. In particular, the largest particle in Fig. 3 is longer than 2 micron, more than

#164938 - $15.00 USD Received 23 Mar 2012; revised 21 Apr 2012; accepted 22 Apr 2012; published 31 May 2012

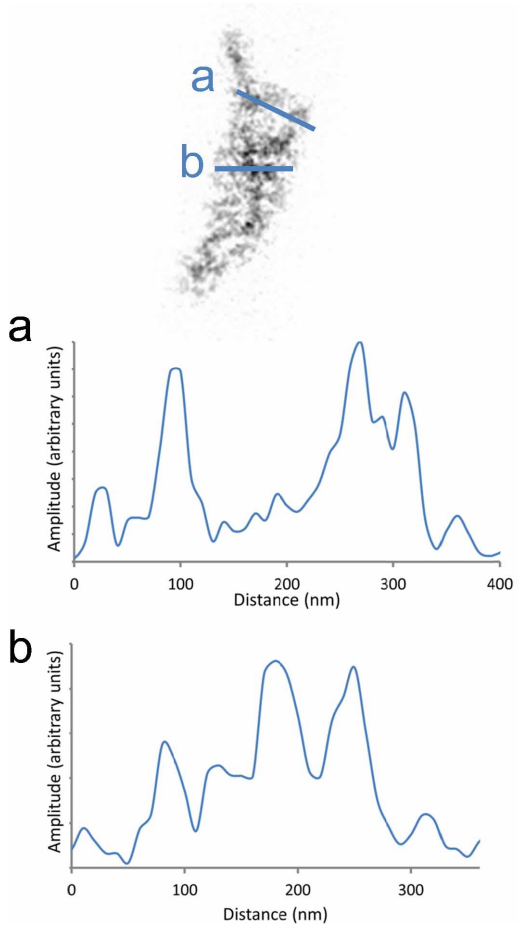

Fig. 4. The bright-field reconstruction of a soot particle shown in Fig. 3 on the fourth row. (a),(b) Line plots from the locations indicated on the image, which show features on the scale of 30-40 nm.

four times larger than previous reconstructions from the LCLS data at the same experimental conditions [1–3].

As a consequence of the experiment geometry, the central speckle is entirely missing in the central hole for particles larger than around 500 nm diameter. Consequently, bright-field reconstructions were not successful without the information from the dark-field reconstructions, as the shrinkwrap algorithm failed to converge to the size and shape of the object. The shrinkwrap method starts with an overestimate of the size of the object, which, if there is missing data, increases the number of unconstrained modes, often preventing convergence.

The dark-field image provided a support and an initial wave function which enabled bright-field reconstructions to be performed, as shown on the right side of Fig. 3. The square root of the dark-field intensity defined in Eq. (5) is used to define the initial wave function of the bright-field reconstruction, because it has a contrast closer to the amplitude of the bright-field reconstruction. The resolution in the bright-field images is higher and reveals finer detail of the complex structure of the soot. Since the initial wave function was not random, multiple reconstructions cannot be used to estimate resolution as conventionally done in CDI. The image

#164938 - $15.00 USD Received 23 Mar 2012; revised 21 Apr 2012; accepted 22 Apr 2012; published 31 May 2012

contains many features on the scale 30-40 nm, as shown in Fig. 4, in agreement with resolutions reported in previous studies [1–3].

As discussed above, bright-field reconstructions are affected by missing modes [8, 22] and this is still true when they are initialized with information from a dark-field reconstruction. Measures were taken to minimize any residual effect of missing data in the bright-field reconstructions shown in Fig. 3. In the upper two reconstructions, overestimated intensity in the gap at high-resolution was attenuated to agree with the radially averaged intensity in the measured data region, providing an excellent visual improvement. The number of missing modes was reduced by the application of a reality constraint, which is appropriate for centrosymmetric diffraction. Loss of centrosymmetry due to Ewald sphere curvature is evident for the two largest particles beyond 60 nm resolution. For the smaller particles, centrosymmetry persists to higher resolutions.

X-ray laser pulses provide the opportunity to study the structures of individual PM2.5 particles in their native airborne state to higher resolutions than optical imaging techniques. Even taking a conservative view of the resolution obtained in this study, these images are the highest resolution ever recorded for airborne PM2.5 that is greater than 500 nm in diameter.

The largest particles imaged in this study approach the dimensions of the beam. Spatial structure in the XFEL pulse can influence the contrast of reconstructed images. Since the spatial structure of the XFEL pulse was not known in this experiment, we are not able to draw any conclusions on this issue. We raise it here, however, to highlight the importance of beam characterization for future XFEL imaging of micron-size particles.

4. Conclusion

Dark-field CDI opens a new route to imaging with coherent radiation that greatly increases the range of particle sizes that can be achieved for a fixed experiment geometry and detector dynamic range without sacrificing resolution. Dark-field CDI provides structural information when missing data complicates standard bright-field reconstruction and turns the curse of missing data into the vehicle for a new contrast mechanism. Besides aerosols, we anticipate dark-field CDI will find application to larger biological samples like cells, bacteria and immunogold-labeled samples.

Note that dark-field images can be formed from existing CDI data because no modification of the experimental set up is required. We expect that using our method, structural information may be recoverable from data previously disregarded as unusable.

Acknowledgments

This work was supported by: the Deutsches Elektronen-Synchrotron, a research center of the Helmholtz Association; the Max Planck Society; the DFG Cluster of Excellence at the Munich Centre for Advanced Photonics; the Virtual Institute Program of the Helmholtz Society; the SLAC Laboratory Directed Research and Development Program. MJB, DNL, DS, CYH, and RGS were supported through by the AMOS program within the Chemical Sciences, Geosciences, and Biosciences Division of the Office of Basic Energy Sciences, Office of Science, U.S. Department of Energy. Experiments were carried out at the Linac Coherent Light Source, a national user facility operated by Stanford University on behalf of the U.S. Department of Energy, Office of Basic Energy Sciences. We thank the staff of the LCLS for their support in carrying out these experiments.

#164938 - $15.00 USD Received 23 Mar 2012; revised 21 Apr 2012; accepted 22 Apr 2012; published 31 May 2012